Published in Journal of Electron Spectroscopy and Related Phenomena 117-118, 2001
which should be used for any reference to this work

On the search for Fermi surface nesting in quasi-2D materials

P. Aebi[a,*], Th. Pillo[a,1], H. Berger[b], F. Lévy[b]

[a]*Institut de Physique, Université de Fribourg, Pérolles, CH-1700 Fribourg, Switzerland*
[b]*Institut de Physique Appliquée, EPFL, CH-1015 Lausanne, Switzerland*

Abstract

We investigate a number of isostructural, quasi-two dimensional transition metal dichalcogenides with respect to Fermi surface nesting. Using angle-resolved photoemission we find no clear evidence for Fermi surface nesting as a key scenario for charge density wave formation in these materials. However, interesting and unusual behavior has been discovered. For *1T*-TaS_2 in the charge density wave phase, instead of finding an intact Fermi surface along the rounded parts of its elliptically shaped contours and gaps along the parallel regions, the Fermi surface is essentially completely pseudogapped. For *1T*-$TiSe_2$ a model based on an excitonic insulator phase as described by Kohn [Phys. Rev. Lett., 19 (1967) 439] fits well with experimental observations. Bandstructure calculations give interesting insight into the electron configuration indicating the changes in d-band occupation and metal-d chalcogen-p overlap when going from one material to the other.

Keywords: Angle-resolved photoemission; Quasi-2D materials; Charge density waves; Fermi surface nesting

1. Introduction

1.1. Angle-resolved photoemission

During recent years angle-resolved photoemission (ARPES) has become increasingly popular as a method for band and Fermi surface (FS) mapping (FSM). Especially for systems where de Haas van Alphen methods [1] are not applicable. Traditionally, in ARPES relatively few energy distribution curves (EDCs) were measured for different angles in order to determine the bandstructure and the parallel momentum ($k_\parallel$) location where bands cross the Fermi level (E_F). Then, Santoni et al. [2] used an alternative way to obtain the same information. With a two dimensional (2D) display-type analyzer they mapped the FS of layered graphite directly by measuring the total intensity within a narrow energy window at E_F. Inspired by Ref. [2] sequential angle-scanning data acquisition [3,4], as introduced by the surface structural X-ray photoelectron diffraction (XPD) method, was used to map the intensities within a narrow energy window at the Fermi energy [5–7]. It was also realized that simple intensity mapping at E_F as a function of angle or $k_\parallel$ might not be sufficient to determine the Fermi vector (k_F) and that a combination of intensity mapping and EDCs is necessary [8]. Another, most important finding was that so-called angular distribution curves (ADCs), i.e. intensities as a function of angle or $k_\parallel$ for a fixed

*Corresponding author. Tel.: +41-26-300-9087; fax: +41-26-300-9747.
E-mail address: philippadrian.aebi@unifr.ch (P. Aebi).
[1]Present address: Institut de Physique, Université de Neuchâtel, Rue A.-L. Breguet 1, CH-2000 Neuchâtel, Switzerland.

binding energy (E_B), are much easier to interpret and fit for quantitative interpretation than the traditional EDCs because of their much simpler line shape [9–12]. The analysis of ADCs instead of EDCs has very recently been applied successfully to the cuprate high T_c superconductors [13]. The present special issue gives certainly an account of the resulting development, even accelerated by drastic instrumental improvements in very recent years.

In ARPES, $k_{\|}$ of the photoelectron is conserved whereas there remains uncertainty as to how well k-perpendicular ($k_{\perp}$) is defined. An ideal case for ARPES is therefore presented when energy dispersion as a function of $k_{\perp}$ is negligible, i.e. for emission from 2D states. Low dimensional systems also exhibit an increased tendency to instabilities and phase transitions, and present, besides interesting material properties, a wonderful playground for physics.

1.2. Transition metal dichalcogenides

Many transition metal dichalcogenides (TMD) exhibit lattice instabilities and charge density waves (CDW). In the present article we consider a series of TMDs, namely $TiTe_2$, $TiSe_2$ and TaS_2, all with the so-called *1T* crystal structure and of the form MX_2, with M the transition metal and X the chalcogen atom. The TMDs are layered materials as shown in Fig. 1 with the metal atoms sandwiched between the chalcogen atoms. Between the sandwiches where the crystals cleave there is a van der Waals gap with reduced interlayer bonding. Therefore, these materials intrinsically have a 2D character and are termed quasi-2D.

In the ionic picture the chalcogen atoms are capturing metal d-electrons. In TaS_2, Ta is nominally left with a single 5d-electron whereas Ti in $TiTe_2$ and $TiSe_2$ nominally remains with no 3d-electrons.

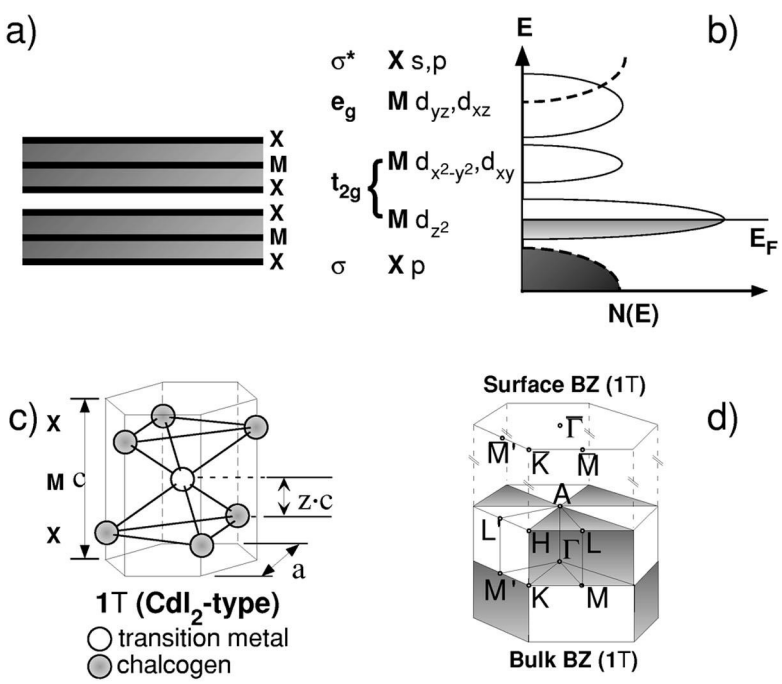

Fig. 1. (a) Sketch of the CdI_2-type *1T* sandwich structure present in *1T*-$TiTe_2$, *1T*-$TiSe_2$, *1T*-TaS_2 and *1T*-$TaSe_2$. (b) Density of states with orbital characters in the ionic picture. (c) Real-space unit cell. (d) Drawing of the bulk and surface Brillouin zones. High-symmetry points are labeled.

The corresponding density of states with crystal field split orbitals is sketched in Fig. 1b. The remaining metal d-electrons at E_F are of dz^2-symmetry. It is also clear that the material properties will be highly sensitive to the number of dz^2-electrons. The lower the number of electrons at E_F, the weaker the screening and the higher the tendency to instabilities. In this regard it seems obvious that the heaviest metal together with the lightest of the chalcogen atoms, i.e. TaS_2, gives the most unstable combination and, on the other hand, $TiTe_2$ the most stable one. Other important factors are the overlap of the metal d-band with the chalcogen p-band and the so-called *z*-parameter as indicated in Fig. 1c. A larger *z*-parameter indicates a larger metal–chalcogen distance. The bulk Brillouin zone (BZ) of the threefold symmetric *1T*-structure as well as the surface BZ (SBZ) with corresponding high-symmetry points is indicated in Fig. 1d.

1.3. Fermi surface nesting

The origin of the CDW instability in these materials is often attributed to FS nesting. The concept of FS nesting is easily understood in 1D. Fig. 2 shows a chain of atoms with distance *a*. If we assume one electron per atom the band is half-filled, i.e. it is filled up to $\pm\pi/2a$, where the BZ extends to $\pm\pi/a$. For the case of a doubled periodicity of $2a$ in real-space the size of the BZ is divided by 2 and extends to $\pm\pi/2a$, i.e. the band is completely filled up to the new BZ boundaries where a gap is opened naturally through the formation of standing waves. Therefore, the system gains electronic energy

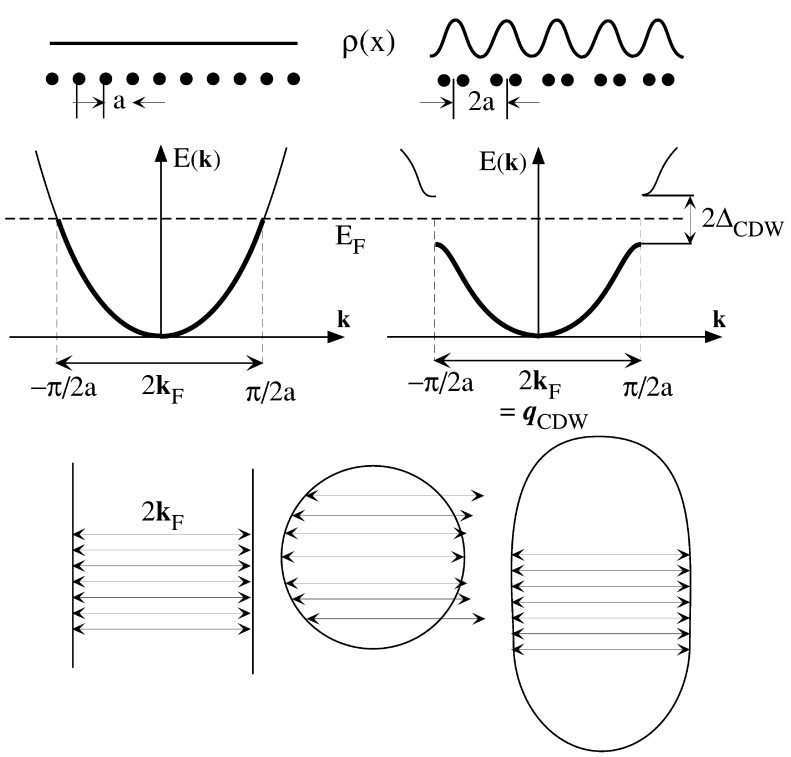

Fig. 2. Charge density wave and Peierls distortion in 1D. A doubling of the periodicity in real-space reduces the extent of the BZ in *k*-space by a factor of 2. A gap opens at the BZ boundary lowering electronic states and allowing to gain energy to compensate for the elastic deformation energy. In 2D the FS has to exhibit a parallel portion in order to be susceptible for an FS nesting scenario based on 1D considerations (see text).

through the lowering of electronic states. This energy is compensated by the elastic energy to be paid for the deformation of the lattice. The CDW wave vector $q_{CDW} = 2k_F$ naturally yields the CDW wavelength of $2a$ via $2\pi/q_{CDW}$. In 1D there are exactly two points to the FS which always connect and the FS is completely nested by q_{CDW}. In a 2D free-electron system the FS is cylindrical (Fig. 2 bottom right) and only two points, an infinitesimal part in this case, are connected for a given q_{CDW}. There is some hope however for elliptically shaped FSs with almost parallel portions. If these portions are large or the coupling between the portions is strong enough, the gain in electronic energy may induce a lattice distortion along the connecting/nesting vector, compensating the distortion energy. Note that the distortion needs not to be commensurate with the underlying lattice.

For our quasi-2D materials, therefore, the FS nesting scenario heavily depends on the particular topology of the FS. In order to detect such a scenario the attention in our experiments has to be directed to parallel parts on the FS contours and within the CDW phase to the opening of an energy gap along these portions and the corresponding appearance of new BZ boundaries.

In the present article we discuss ARPES and FSM measurements and resistivity data on *1T*-TaS_2 and *1T*-$TiSe_2$. Most of the experimental photoemission data have been taken from Refs. [14–17]. For a detailed discussion of previous ARPES experiments by other authors and their consequences for different models we therefore refer the reader to these references. Here the experiments are complemented by bandstructure calculations on *1T*-TaS_2, *1T*-$TiSe_2$, *1T*-$TiTe_2$ and *1T*-$TaSe_2$.

The next section gives a description of experimental procedures and calculations. In Section 3 follow results and discussion including subsections on *1T*-TaS_2, *1T*-$TiSe_2$ and bandstructure calculations. Section 4 ends with a summary and conclusions.

2. Experiments and calculations

The measurements were performed in a VG ESCALAB Mk II spectrometer modified in order to enable motorized sequential angle-scanning data acquisition [3,4]. Photoelectrons excited with monochromatized He Iα (21.2 eV) radiation [18] were analyzed with a 150-mm-radius hemispherical analyzer. The base pressure was 2×10^{-11} mbar and the uncorrected He partial pressure during operation reached 7×10^{-9} mbar. ARPES and FSM experiments were performed with an energy and angular resolution of 20 meV and $\pm0.5°$, respectively.

Pure *1T*-TaS_2 samples were prepared by standard flux growing techniques [19,20]. All *1T*-TaS_2 samples showed clear first order phase transitions at 180 K [21] indicating very good crystal quality. *1T*-$TiSe_2$ was prepared with the chemical vapor transport method [22]. Best samples were grown at 500°C with ICl_3 as transport agent. These samples showed the best stoichiometry and resistivity ratios $\rho(165\ \mathrm{K})/\rho(295\ \mathrm{K}) = 3.3$. All samples were grown in the presence of a slight Se excess [22,23]. In addition, Hall coefficient measurements revealed, that above the transition at ~180 K, conduction is p-type, i.e. from holes, and below n-type, i.e. from electrons [22] in accordance with other measurements [24].

Sample cleavage was carried out in situ using adhesive tape at a pressure in the 10^{-11} mbar range. The crystals were oriented in situ with XPD which provides accurately high-symmetry directions. Surface quality and cleanness have been checked by low energy electron diffraction (LEED) and X-ray photoelectron spectroscopy, respectively.

Experiments were performed basically in two different modes. Firstly, angle-scanning of photoelectron intensity at a constant energy such as E_F, or slightly below and above. Briefly, in such an FSM experiment, the spectral function in a small, resolution-limited energy window is scanned over nearly 2π solid angle and represented in a gray-scale plot mapped as a function of $k_\parallel$. Secondly, angles are scanned on a dense grid as in the first mode but instead of recording intensity at single energies complete EDCs are collected. These modes are well established, and have proven their power on many material systems [7,8,12,15,25]. For a review see Ref. [26].

We also performed bandstructure calculations for the different compounds using the full potential linearized augmented plane wave (FLAPW) method [27] in the framework of the generalized gradient approximation [28]. The lattice parameters of the D^3_{3d}

space group materials were chosen from Ref. [29] for *1T*-TaS_2, *1T*-$TiSe_2$, *1T*-$TiTe_2$ and from Ref. [30] for *1T*-$TaSe_2$. For comparison with the experiment, we assumed a free-electron final-state. Energy eigenvalues were calculated along the free-electron final-state momenta and a linear gray-scale is used to indicate energy conservation.

3. Results and discussion

In Fig. 3 we present a compilation of bandstructure calculations and resistivity curves for $TiTe_2$, $TiSe_2$, TaS_2 and $TaSe_2$, all with the *1T* structure. Arrows A and B in the bandstructure indicate the transition metal-dz^2 and chalcogen p-bands, respectively. The resistivity measurements have been taken from Claessen [31], Lévy [23], DiSalvo et al. [32] and DiSalvo et al. [32], for *1T*-$TiTe_2$, *1T*-$TiSe_2$, *1T*-TaS_2 and *1T*-$TaSe_2$, respectively. *1T*-$TiTe_2$ behaves like a normal metal whereas the others exhibit phase transitions. Note that $TiTe_2$ is considered as the prototype for a Fermi liquid of correlated electrons forming quasi particles (QP) and ARPES displays all the expected behavior [33]. Except *1T*-$TiTe_2$ all three compounds exhibit CDWs. *1T*-TaS_2 even has multiple transitions and appears as the most unstable of the materials. It has quite a complicated phase diagram with an incommensurate (IC) CDW phase below 540 K, a quasi-commensurate (QC) CDW phase below 350 K and a commensurate phase below 180 K. *1T*-$TaSe_2$ is similar to *1T*-TaS_2 but much simpler. It has the same CDW ($\sqrt{13}\times\sqrt{13}$) symmetry but only a single commensurate phase. For *1T*-$TiSe_2$, lowering the temperature from room temperature (RT) increases the resistivity to a maxi-

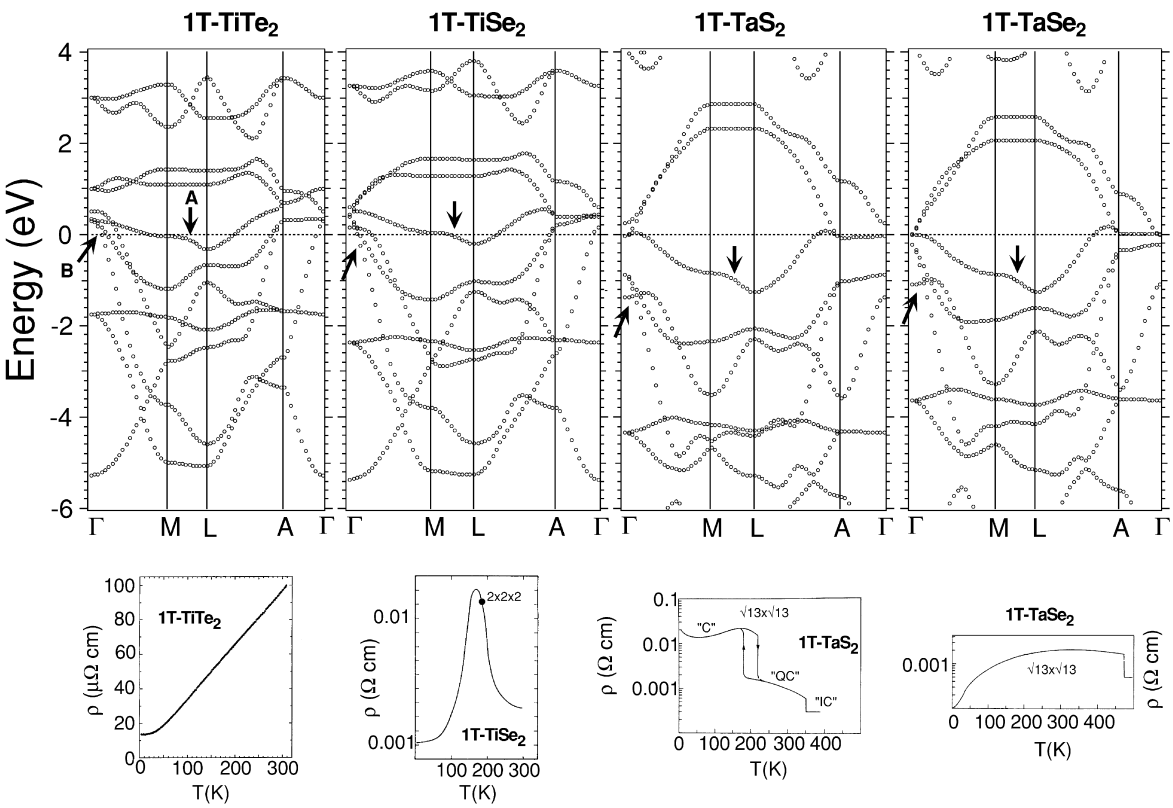

Fig. 3. Bandstructures and resistivity curves for *1T*-$TiTe_2$, *1T*-$TiSe_2$, *1T*-TaS_2, *1T*-$TaSe_2$. Resistivity data have been taken from Claessen [31], Lévy [23], DiSalvo et al. [32] and DiSalvo et al. [32], for *1T*-$TiTe_2$, *1T*-$TiSe_2$, *1T*-TaS_2 and *1T*-$TaSe_2$, respectively. Bandstructures have been calculated using WIEN97 [27].

mum value at ~180 K ($T_{\rho\max}$) and decreases again to reach better conductivity than at RT. However, before reaching $T_{\rho\max}$ the CDW sets in with a ($2\times 2\times 2$) symmetry, i.e. the lattice periodicity is doubled in all directions.

3.1. 1T-TaS_2

At RT we find the QC CDW phase. This is a phase where the CDW is commensurate but there are only small domains of the order of 60 Å with no phase coherence [34,35]. Below 180 K resistivity increases by an order of magnitude and the CDW phase becomes coherent. The CDW symmetry in real-space is indicated in Fig. 4a. According to the model by Fazekas and Tosatti [36,37] little stars of 13 Ta atoms form consisting of a center atom, an inner and an outer ring of six atoms each. The resulting ($\sqrt{13}\times\sqrt{13}$)-R13.9° reconstruction is well present at RT in the QC-phase as seen in the RT LEED pattern in Fig. 4b. Fig. 4b also shows the corresponding unreconstructed and reconstructed BZs. As the temperature is lowered below 180 K Ta d-electrons localize and an upper and lower Hubbard band is formed as indicated in Fig. 4c [36,37]. The metal–insulator transition removes the FS and resistivity drastically increases. Normal emission photoemission in Fig. 4d nicely shows the downward shift of the lower Hubbard band when going from the QC to the C-phase. Remarkable is the splitting of the band into at least three distinct peaks. Following Fazekas and Tosatti [36,37] these peaks correspond to the splitting of the dz^2-band due to the different shells of the little stars in Fig. 4a.

The interesting question is what happens to the FS. Fig. 5 shows calculated cuts across the FS. In Fig. 5a a spherical cut is displayed according to the free-electron final-state indicated in Fig. 5b. A cartoon of the 2D FS is drawn in Fig. 5c as deduced from horizontal cuts across the hexagonal BZ at

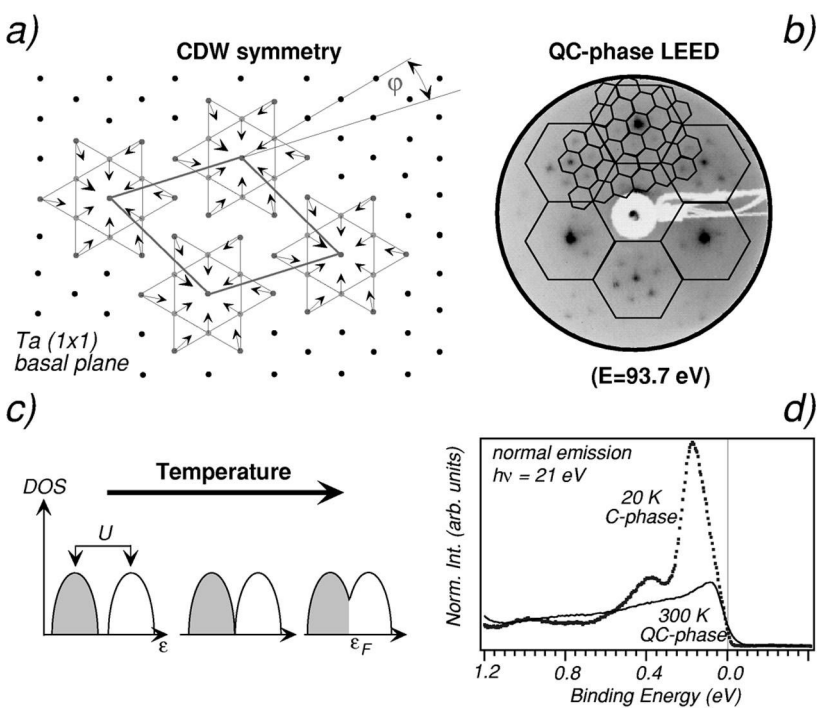

Fig. 4. (a) Ta (1×1) basal plane with small stars caused by the ($\sqrt{13}\times\sqrt{13}$)-superstucture of the CDW phase. The arrows indicate the lattice distortions on the Ta sites. The new real-space unit cell is given by the rhombus. (b) Low energy electron diffraction (LEED) pattern of the QC-phase ($E_{\rm kin}$ 93.7 eV). The unreconstructed SBZ and the superstructure SBZ are indicated by the large and small hexagons, respectively. (c) Upper and lower Hubbard band separated due to localization of Ta d-electrons with Coulomb repulsion *U*. (d) Synchrotron radiation ($h\nu = 21$ eV) normal emission spectrum taken from the QC and the C phase.

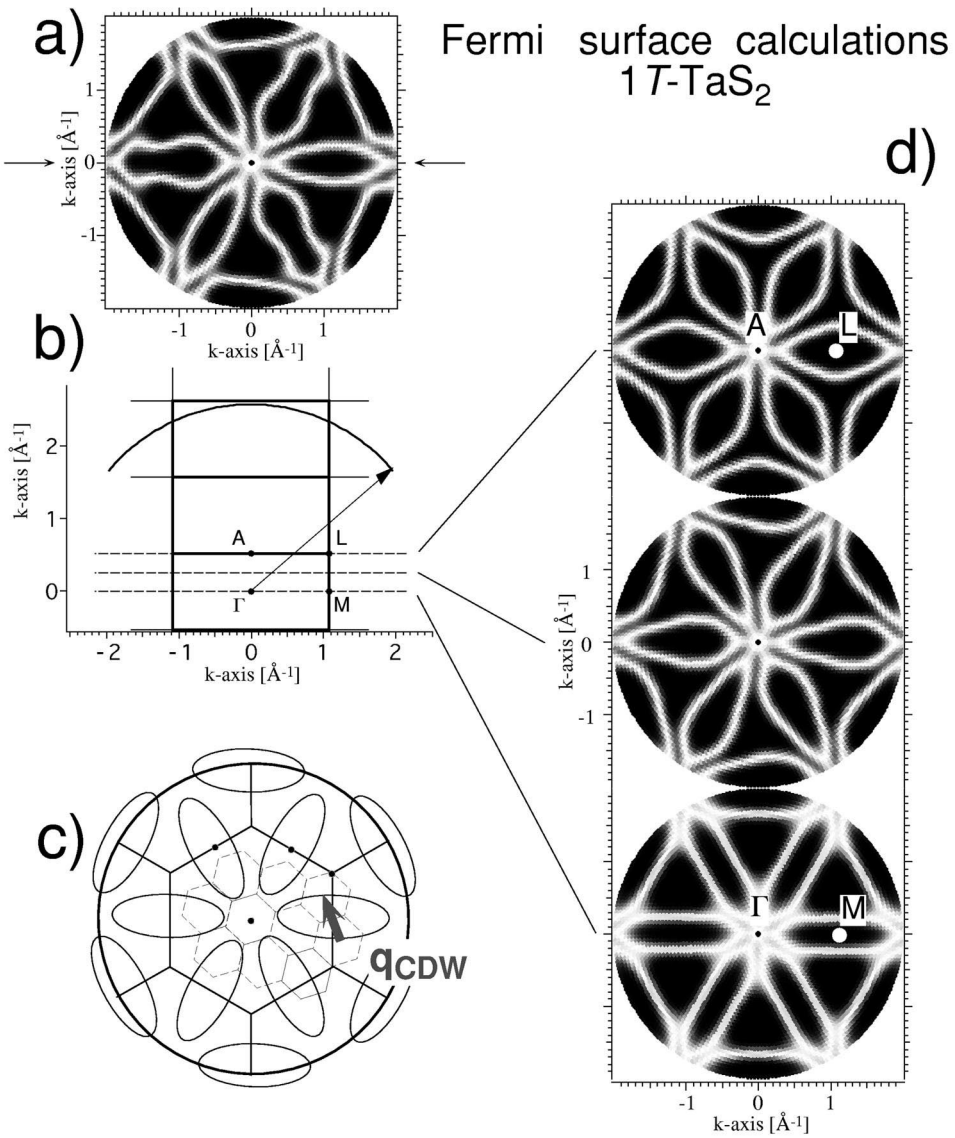

Fig. 5. (a) Calculation assuming the free-electron final-state displayed in (b) using photon energy of 21.2 eV, an inner potential of 10 eV, and a work function of 4.6 eV. (b) BZs in the ΓALM plane in the extended zone scheme, FS contours and free-electron final-state k-points assumed for (a). (c) Cartoon of the FS calculated in (d) for different cuts. It includes the (1×1) and ($\sqrt{13}\times\sqrt{13}$) BZs and a possible nesting vector corresponding to the CDW wave vector q_{CDW}. (d) Calculated FS cuts for planes differing in $k_{\perp}$ as indicated in (b).

different levels in Fig. 5d. The calculations have been done for the undistorted (1×1) lattice. From the ($\sqrt{13}\times\sqrt{13}$)-R13.9° reconstruction new, smaller BZs are expected as indicated in Fig. 5c. The ellipses consist of electron pockets as can be seen from the bandstructure calculations displayed in Fig. 3. Following the ΓM or AL directions in Fig. 5b we find two E_{F} crossings. The calculated cuts indicate a threefold symmetry consistent with the BZ shown in Fig. 1d. Comparing the calculated FS with the sketch in Fig. 2 (bottom right), at RT we would expect an intact FS with gaps along the flat regions, since at RT the CDW is present. Furthermore q_{CDW} fits more or less within the flat parts of the elliptical contours

(Fig. 5c). However, nesting is certainly far from perfect and the horizontal FS cuts clearly indicate a $k_\perp$ dependence with truly flat portions only along ΓM, but with a connecting vector that does not fit q_{CDW} anymore. Therefore the sketch (Fig. 5c) is useful only for illustration purposes. The $k_\perp$ dependence can also be appreciated from the modulation of the FS contours along the perpendicular direction in Fig. 5b since for a truly 2D system these contours would be straight lines.

The RT FSM experiment of the QC CDW phase is shown in Fig. 6a. Very high intensity is measured

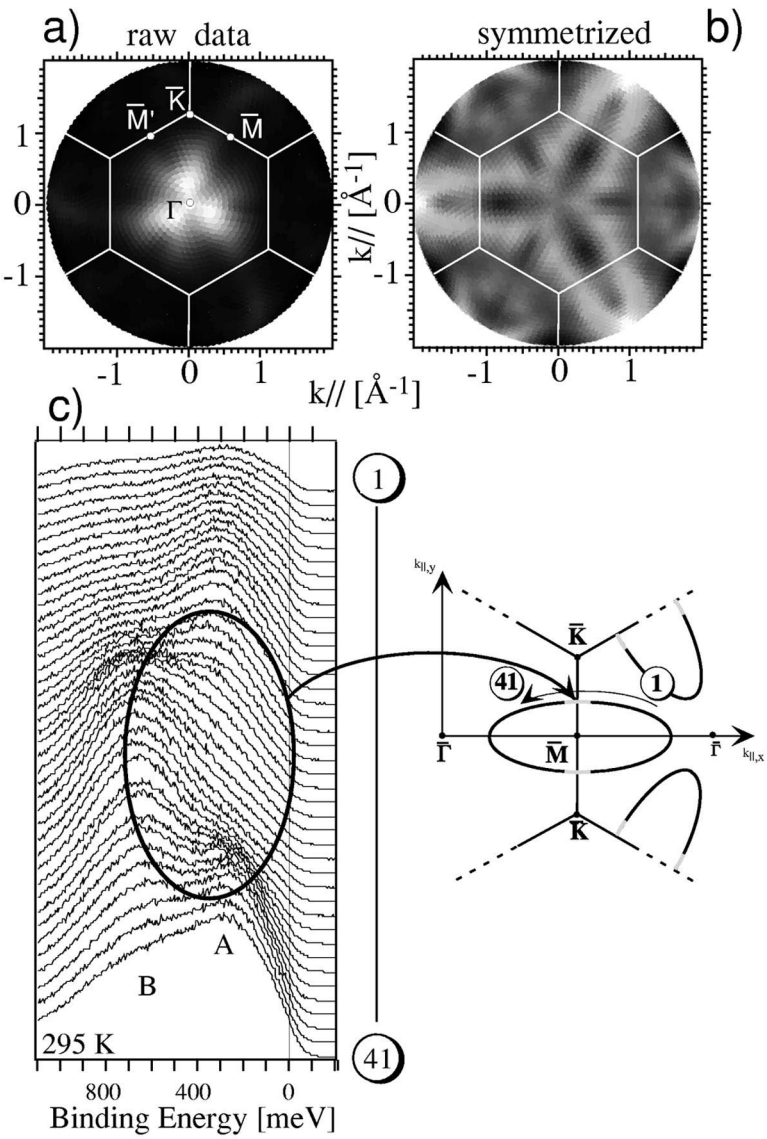

Fig. 6. (a) RT angular distribution of electrons from E_F mapped as a function of $k_\parallel$. White and black corresponds to high and low intensity, respectively. The (1×1) BZ and high-symmetry points are indicated. (b) Symmetrized and flattened data of (a), see text. ARPES spectra taken along one branch of the high-intensity contour around $\bar{M}$ as indicated in the sketch to the right. Enumeration of spectra is shown at the right by an arrow. Raw data are shown without normalization. The spectra are composed of two main peaks A and B. Marked is the area of depressed intensity of peak A.

near normal emission with a strong fall-off for higher emission angles. This fall-off is expected from matrix element effects for emission from dz^2-orbitals and the effect may even be stronger due to the localized character of dz^2-electrons in TaS_2: the matrix element for a dipole transition from a localized orbital into a free-electron final-state gives the Fourier transform of the initial-state wave function [38]. Therefore, the angular dependence is proportional to $|Y_{20}(\theta_k, \phi_k)|^2$ where $Y_{20} = \sqrt{(5/16\pi)}(3\cos^2\theta - 1)$ is the spherical harmonics with dz^2-character and θ_k and ϕ_k the polar and azimuthal emission angle, respectively. Consequently, intensity is strongly decreasing with increasing emission angle θ_k. In order to visualize the intensity distribution within the dark regions Fig. 6b shows a treated image. The data has been averaged according to the D^3_{3d} space group and divided by the mean intensity on every polar emission angle in order to amplify the dark regions. As a result high-intensity contours appear in Fig. 6b. The first point to notice is that there is no apparent new symmetry due to the $(\sqrt{13}\times\sqrt{13})$-R13.9° superstructure. The reason for this is unclear. It may be that the Fourier components of the potential for electrons with energy corresponding to E_F are too weak to have an effect.

Since high intensity along contour lines does not necessarily ascertain the E_F crossing of a QP, spectra have been measured along one branch of the elliptically shaped contour centered around $\bar{M}$ in Fig. 6a. The spectral shape is dominated by two main peaks A and B (Fig. 6c), a third close to E_F may be hidden. We notice two important points. Firstly, there is strongly suppressed intensity or spectral weight in the region where we expect nesting. Secondly, intensity at E_F (zero binding energy) is very weak all along, indicating that there may not be a QP crossing on this contour at all.

In order to see how to detect a QP crossing E_F in ARPES, Fig. 7a shows a series of spectra taken for *2H*-$TaSe_2$ (not *1T*-TaS_2) along the $\bar{\Gamma}\bar{M}$ direction. It is also the Ta d-band as in *1T*-TaS_2 that is investigated although in a different environment and we clearly observe a QP crossing E_F. This is manifest through the midpoint of the leading edge shifting above E_F and an accompanying drop of peak intensity. The drop is explained by the Fermi–Dirac cut-off of the QP spectral weight and the midpoint shift by the QP being located just above E_F pushing the cut-off towards higher energies. The same experimental scan for *1T*-TaS_2, Fig. 7b, does not indicate a crossing in this sense since the midpoint of the leading edge always stays below E_F. One broad dispersing QP peak is observed which might be on top of up to three quasi-localized features that can be explained within the Fazekas and Tosatti model [36,37]. The calculation displayed as gray-scale plot (Fig. 7c) clearly shows a crossing which is also evident from the bandstructure calculation in Fig. 3. For comparison, the experiment of Fig. 7b is also plotted as a gray-scale intensity map (Fig. 7d).

In order to corroborate this non-crossing behavior, in Fig. 8, azimuthal scans have been measured perpendicular to the $\bar{\Gamma}\bar{M}$ direction cutting across the high-intensity contours. The scan direction is indicated in Fig. 8a (bottom right). Two main peaks A and B dominate the spectral shape as can be seen in Fig. 8b. The two peaks are most dominant at the extreme positions (i.e. the top and bottom most spectra) where they can be compared to the spectra taken along the contour shown in Fig. 6c and merge to one dominant peak in the center (marked by a black dot) where the spectra can be compared to the ones in Fig. 7b. Observing the gray-scale plots in Fig. 8a we find that the apparent dispersion indicated by small white dots remains within a certain bandwidth given by the width of peaks A and B but reflects in width and depth the position within the ellipse, i.e. the closer to the center ($\bar{M}$-point in Fig. 8a, bottom right) the scan is located the wider and deeper the U-shaped dispersion of the white dots appears. If, however, we observe intensity we find that as we go from $k_{\parallel} = 1.56$ to $k_{\parallel} = 1.40$ the peak intensity switches from A to B. The same observation is made from Fig. 8b. This is also the region in Fig. 6c where peak B gains weight upon peak A. Remaining with Fig. 8b and observing the center spectrum we notice that the peak intensity switch from A to B simply goes along with the downwards movement (in energy) of the peak maximum of the center spectrum marked with a black dot. This peak maximum follows (in energy) the dispersion shown in Fig. 7b resembling nicely the single particle calculation Fig. 7c. Therefore, dispersion appears single particle like inside the elliptical contours and quasi-localized outside as also seen from the disper-

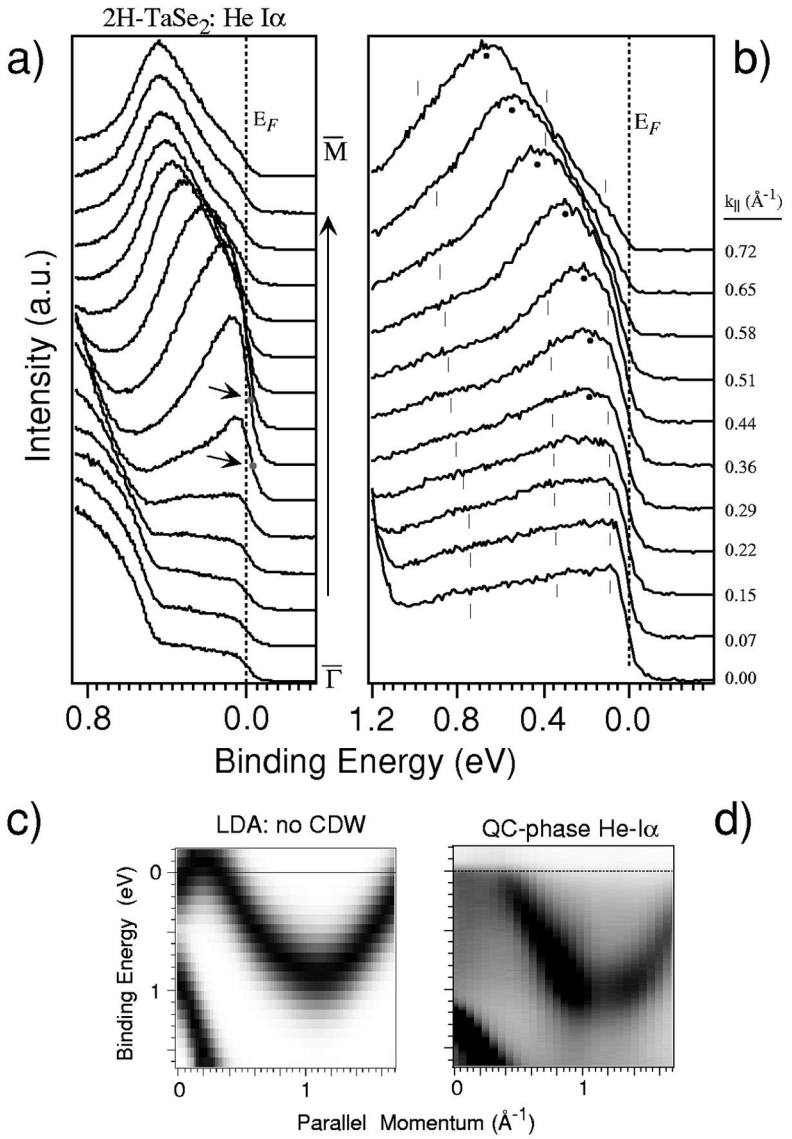

Fig. 7. (a) *2H*-$TaSe_2$ ARPES along indicated direction. Notice the shifting of the midpoint of the leading edge of the Fermi–Dirac cut-off towards energies above E_F, and the sudden peak intensity drop. Both indicate the QP crossing E_F. (b) The same as (a) but for *1T*-TaS_2. No evidence for QP crossing. Small ticks and black dots are a guide to the eye and indicate CDW-induced satellites and QP positions, see text. (c) Calculated dispersion plot in the ΓALM-plane for *1T*-TaS_2. (d) Experimental dispersion plot in the ΓALM-plane for *1T*-TaS_2. Same data as in (b) but covering a larger region. Black and white indicate high and low intensity, respectively.

sionless behavior at the border of the gray-scale plots in Fig. 8a.

As a result of this dense *k*-space mapping we gain quite a complete picture of an, obviously, peculiar behavior of *1T*-TaS_2 in the QC CDW phase at RT. It is summarized in Fig. 8c. The FS appears pseudo-gapped and remnant, i.e. there is strongly reduced spectral weight at E_F without clear QP crossing, with a maximum intensity distribution reflecting the calculated (1×1) single particle FS. The dispersion behavior is a mixture of single particle dispersion within the elliptical contour and localization by the

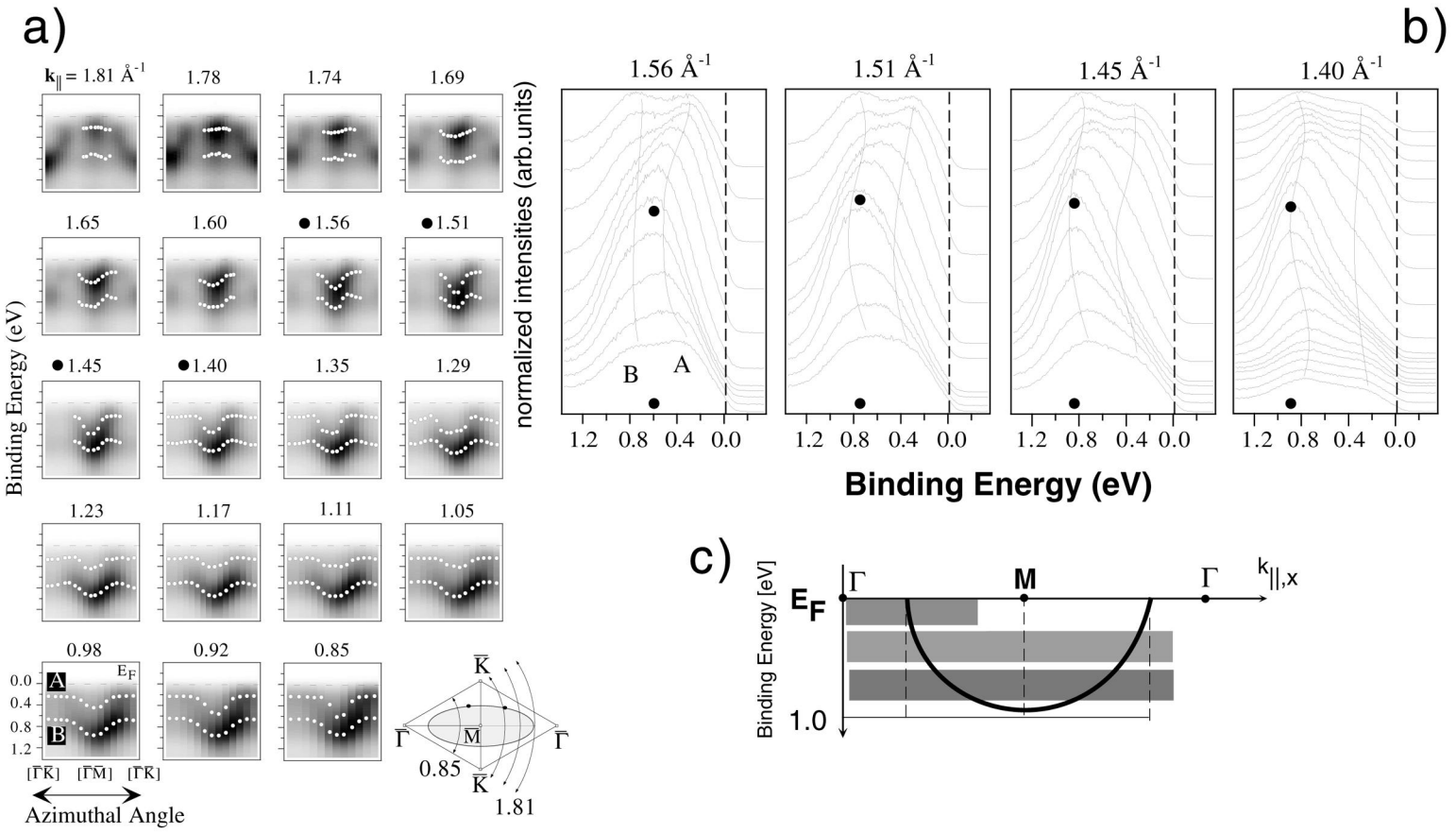

Fig. 8. (a) Azimuthal ARPES sections through the 2nd and the 1st SBZ for different parallel Aebi, Philipp ; Institut de Physique, Université de Neuchâtel, Switzerlandmomenta, taken with $h\nu = 21.2$ panel. The dashed line gives the Fermi level. Bottom left: energy and momentum scale valid for all panels. Bottom right: sketch of the location where spectra have been taken. (b) Selected ARPES spectra from the panels of (a) for parallel momenta from 1.56 to 1.40 Å. The two lines are a guide to the eye for the observed dispersion of peaks A and B. Black dots indicate the main peak position of the center spectrum. (c) Cartoon of the peculiar dispersion behavior with single-particle dispersion and CDW-induced localization, see text.

CDW-induced splitting of the d-band outside. For this reason it is difficult to interpret the spectral weight loss in Fig. 6c as due to the opening of a CDW gap as expected for an FS nesting scenario, rather, it may be a consequence of this peculiar dispersion behavior. Nevertheless, it cannot be ruled out. It is interesting to speculate why the Fermi surface is pseudogapped. A tempting explanation is that the underlying instability, i.e. a Mott localization derived transition [36,37] leading to a commensurate CDW phase at 180 K, is responsible via fluctuations, that are present already above T_c. This is similar to what has been found in underdoped cuprates at temperatures around T_c [39]. There, a crossover temperature $T^* > T_c$ has been introduced where a pseudo-gap opens above the underlying superconducting transition as an instability.

3.2. 1T-$TiSe_2$

For *1T*-$TiSe_2$ the situation appears completely different. Already from the band structure calculation, Fig. 3, we realize that both, the metal and the chalcogen atoms are involved with the FS. The FS should be composed of hole-pockets around Γ and electron-pockets around L. Fig. 9a shows the constant energy mapping of electrons with $E_B = 20$ meV. The observed pattern does not change significantly for different binding energies within ~100 meV [16]. The spots vary slightly in size. Again we question whether there is a real FS. Why is there a CDW? There are certainly no parallel portions where we could expect a nesting mechanism. Having the example of TaS_2 in mind and knowing that mapping imperatively has to be combined with taking spectra, Fig. 9b displays dispersion plots along the ΓM direction above the phase transition at RT and below at ~140 K. At RT the Se 4p hole-band appears occupied and most interestingly the Ti 3d electron-band is only thermally occupied, and, without normalization, dispersion is visible, which is quite unusual for ARPES. The dispersion of states above E_F seen without normalization requires a flat dispersion and a narrow peak width [16]. Because of $k_\perp$ dispersion we cannot determine the absolute energy position of bands and one has to rely on synchrotron radiation studies and bandstructure calculations. In a synchrotron radiation study with variable photon energy Anderson et al. [40] determined the $k_\perp$ dispersion of the Se p-bands and found that they are slightly unoccupied (~15 meV) providing a small hole pocket around Γ. From their experiment we also conclude that with our photon energy we are close to the A-point of the bulk BZ. In their article they also provide an inner potential which allows to calculate the *k*-space location at a given angle within the free-electron final-state approximation. The situation is displayed in Fig. 9c. Comparing with the band-structure calculation in Fig. 3 we notice however that at the A-point the band closest to E_F is empty. This is in contradiction with the measurements and also with the calculation of Zunger et al. [41] where the band is occupied near A. The reason for this discrepancy is not known. For the L-point the bandstructure calculation indicates that the Ti 3d-band reaches its lowest energy. Since our measurement passes near the L-point the Ti 3d-band is truly above E_F and only thermally occupied. As a consequence there seems to be a small overlap in energy position between holes at Γ and electrons at L. The spanning vector between Γ and L exactly corresponds to the $(2\times2\times2)$ superstructure observed for temperatures below ~200 K. At low temperature the dispersion plot (Fig. 9b) reveals a lowered Ti 3d-band and a Se p-band which has undergone an umklapp according to the new symmetry. This behavior, together with the resistivity fits surprisingly well with the excitonic insulator scenario proposed by Kohn [42] and sketched in Fig. 10. If the number of carriers is sufficiently small, the screening of the Coulomb interaction between electrons and holes is weak. However, an unscreened Coulomb interaction will always lead to a weakly bound electron–hole pair, i.e. an exciton. In the case of a semimetal or semiconductor with a small indirect (negative or positive) band gap, excitonic phases may occur under several conditions. Firstly, there has to be a reconstruction which doubles the periodicity of the lattice [42]. This first condition is fulfilled. The second condition is the very existence of two bands, an electron-band and a hole-band at different locations in *k*-space with an indirect gap. In our case (Fig. 10) the Se 4p-band is partly unoccupied. The dashed area denotes the occupied part. The horizontal line denotes the Fermi level. At the L-point, the Ti 3d-band

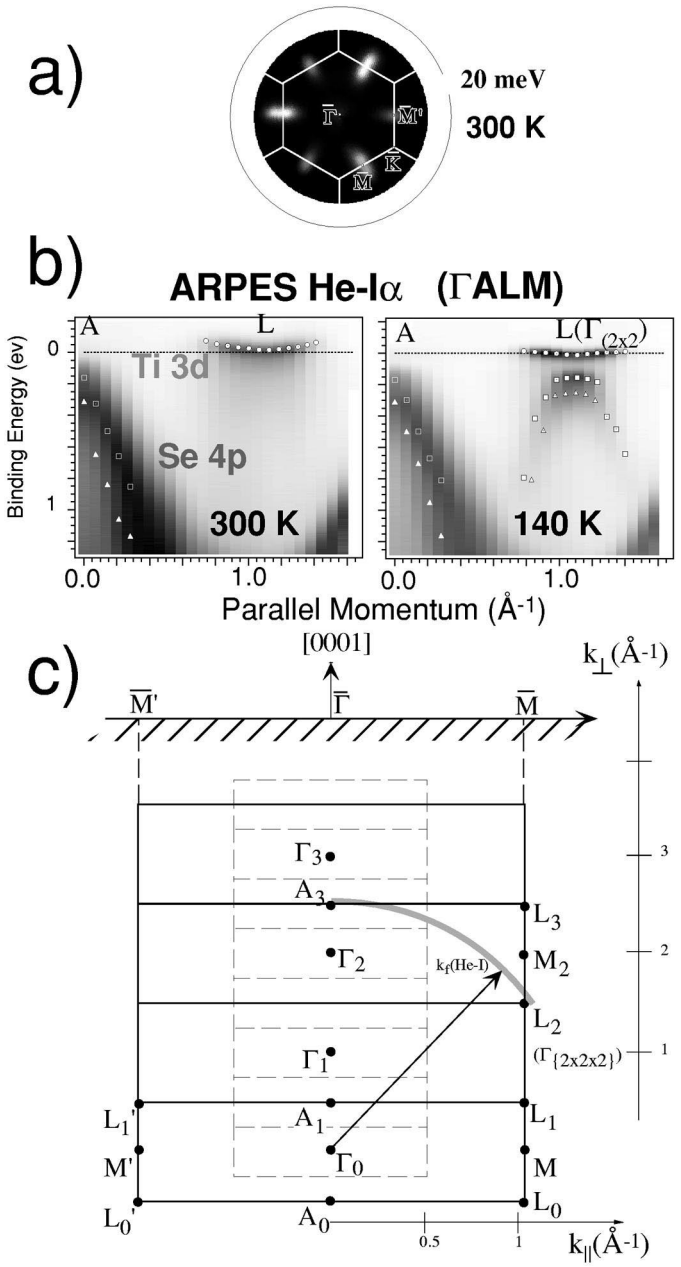

Fig. 9. (a) Constant energy ($E_B = 20$ meV) intensity mapping of *1T*-$TiSe_2$, performed at RT with He-I radiation. (b) Complete ARPES sets for the ΓALM plane, at RT (left) and at 140 K (right). Modeled peak positions are superposed for the Ti 3d-bands as well as for the Se 4p-bands at the respective temperatures. (c) Sketch of the situation in *k*-space. The free-electron final-state vector is given as a gray circular trajectory. An inner potential of 10 eV is assumed and the measured work function is 4.6 eV. Unreconstructed Brillouin zones (BZs) are given as black rectangles, reconstructed BZs are depicted as dashed rectangles. The corresponding surface BZ is given.

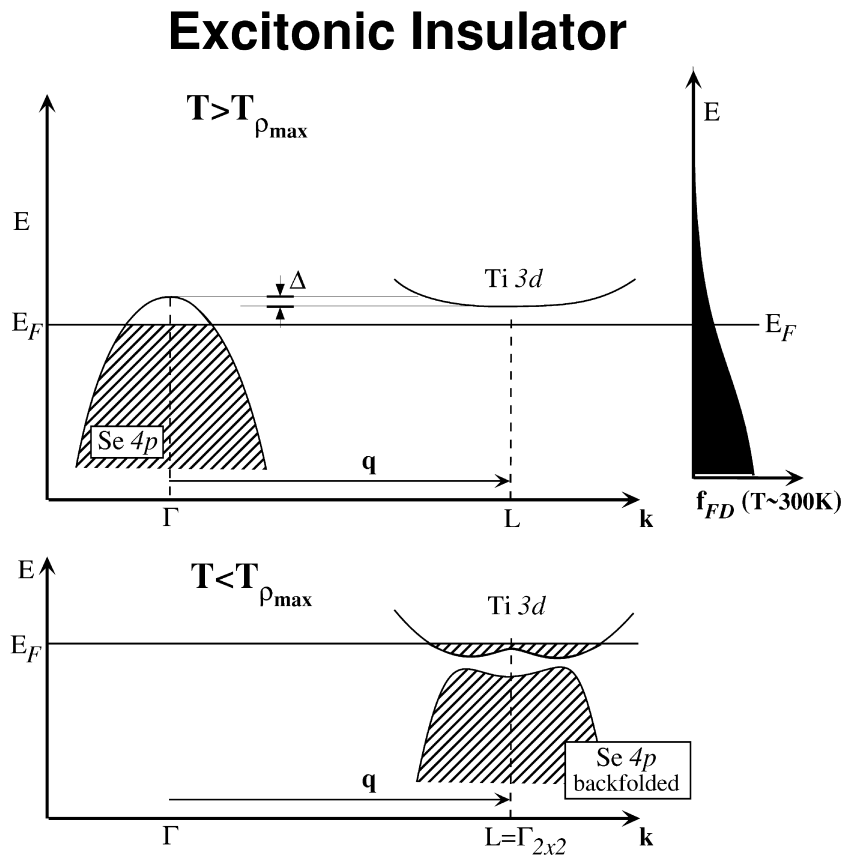

Fig. 10. The excitonic insulator phase according to Ref. [42]: (top) the situation before the phase transition $T > T_{\rho\max}$ and (bottom) the situation after the second order phase transition for $T < T_{\rho\max}$, implying the required (2×2) reconstruction with spanning (not nesting!) vector q. Δ indicates the indirect gap (negative or positive) of the electron and hole-bands (see text).

has its energy minimum slightly above E_F. The resulting overlap, Δ, is of the order of several meV and of the order of the exciton energy [16]. In order to visualize the extent of the band filling with respect to thermal population we also display a Fermi–Dirac distribution at $T = 300$ K. Below the transition temperature the situation at L dramatically changes. The Se 4p is back folded and the Ti 3d-band is shifted down. The experimentally observed situation is in perfect agreement with the picture presented by Kohn for the occurrence of the excitonic phase [42]. Furthermore, transport data [22] indicates a positive Hall coefficient with holes as the major type of charge carriers switching to negative below $T_{\rho\max}$. This fits well with our observations where above the transition we have a thermally occupied electron-band with probably only few electrons, thus a majority of holes. As temperature is lowered the Ti 3d-band becomes occupied providing more and more electrons up to the point of equality of electrons and holes but also of maximal number of excitons and corresponding maximum resistivity. As temperature is lowered even further and presumably also the Ti 3d-band, more electrons are provided switching the sign of the Hall coefficient and also improving conductivity.

3.3. Bandstructure

There are a number of open questions. ARPES has provided a sort of phenomenology that can be

compared with different scenarios. Bandstructure calculations may be useful to get specific answers but since their results do not perfectly fit experiments their answers may be questioned. All sorts of uncertainties exist such as what role the surface plays, to what extent is the free-electron final-state an acceptable approximation, and, of course, what is the influence of matrix elements. Furthermore, experiments should be even more elaborate in what concerns resolution and temperature control.

Why, for instance, are some of the materials unstable and others not or to a lesser extent. *1T*-$TiTe_2$ does not show a phase transition, *1T*-$TiSe_2$ does. *1T*-TaS_2 has many transitions and undergoes a metal insulator transition, *1T*-$TaSe_2$ 'only' shows a single CDW phase. Why, with temperature the Ti 3d-band lowers its energy, changing overlap with the Se 4p-band.

Bandstructure calculations as shown in Fig. 3 may give an indication to what extent a material is susceptible to instabilities. Comparing the four bandstructures in Fig. 3 we notice that they are quite similar. Near E_F, there is the metal d-band (marked by arrow A) and the chalcogen p-band (arrow B). What changes, is the relative position, the occupation and the bandwidth. In the Ti-containing compounds the ionic occupation of the Ti d-band is zero whereas for Ta it is one. This explains the difference between the Ti- and Ta-containing materials. The difference between *1T*-$TiTe_2$ and *1T*-$TiSe_2$ is that *1T*-$TiTe_2$ has a much increased d–p overlap and also the Ti 3d-band appears with a higher occupation. This indicates more charge carriers, better screening and more stability.

With respect to the question why the Ti 3d-band comes down with temperature in *1T*-$TiSe_2$, a calculation with a reduced lattice constant results in a lowering of the Ti 3d states. Therefore, this lowering in energy might be a consequence of the lattice contraction with temperature.

The characteristics of *1T*-TaS_2 is that the Ta d-band is practically completely isolated with negligible overlap with the S p-band. This isolation is definitely not present in *1T*-$TaSe_2$ since the Se p-bands reach practically up to E_F (arrow B). Therefore the d-electrons may be less susceptible to localization. The CDW-induced lattice distortion probably disturbs the interaction and overlap between neighboring Ta d-electrons in *1T*-TaS_2 therefore favoring localization of these electrons. This is hindered in *1T*-$TaSe_2$ probably because of the interaction of Ta d-electrons and Se p-electrons. The initial reason for the occurrence of the CDW, however, is not known. It may still be that nesting on the elliptically-shaped FS plays a role. For this, it is necessary to do ARPES experiments at temperatures above the CDW transition temperature, which is difficult since it is close to the non-reversible phase transition into the *2H* structure, or, to do experiments on *1T*-$TaSe_2$ which does not exhibit the metal–insulator transition but only the CDW with identical ($\sqrt{13}\times\sqrt{13}$) symmetry. An RT experiment in the CDW phase, then, should show a nested and partially gapped but otherwise intact FS if the nesting scenario is true. This would also tell us whether it is true that the underlying metal–insulator transition, via fluctuations, is responsible for the pseudogapped character of the FS of *1T*-TaS_2. Another way to vary the d–p overlap would possibly be the intercalation of alkali metal atoms into the van der Waals gap.

Another interesting point to notice deals with the dimensionality of the material. On the one hand there is this van der Waals gap and the fact that the crystals cleave easily between the chalcogen planes. But, on the other hand bandstructure calculations show quite a strong $k_\perp$ dispersion for some bands along ΓA. This means that there is interaction and orbital overlap across the van der Waals gap but no net bonding. We can understand this in terms of bonding and antibonding orbitals, both being occupied, compensating each other but each exhibiting remarkable $k_\perp$ dispersion. For the *1T*-$TiSe_2$, temperature-dependent experiments across the phase transition would be interesting in order to monitor the shifting down of the Ti 3d-band continuously. Furthermore, there is the intriguing question whether excitons would be observable at $T_{\rho\max}$.

4. Summary and conclusion

Using angle-resolved photoemission including Fermi surface mapping we have investigated a series of transition metal dichalcogenides. No clear evidence has been found for Fermi surface nesting

being responsible for creating the charge density wave. However, other interesting and unusual behavior has been discovered.

1T-TaS_2, at room temperature, is in a so-called quasicommensurate charge density wave phase. According to the Fermi surface nesting scenario, the expectation is to find a Fermi surface which is intact except for small areas where Fermi surface nesting induces reduction or removal of spectral weight. Surprisingly, Fermi surface mapping experiments show that the Fermi surface is essentially completely pseudogapped, i.e. there is spectral weight at E_F but there are no quasiparticles crossing E_F [15]. The spectral weight at E_F is maximal at *k*-space locations within the Brillouin zone where the normal state Fermi surface is expected as it can be calculated (using the local density approximation) for undistorted, metallic TaS_2. Therefore, a sort of remnant Fermi surface is observed. *1T*-TaS_2 can be compared to similar transition metal dichalcogenides such as *1T*-$TiTe_2$ and *1T*-$TiSe_2$ with the same *1T* structure. Whereas *1T*-$TiTe_2$ does not show any transition, *1T*-$TiSe_2$ follows the scenario of the excitonic insulator phase proposed by Kohn [42]. Bandstructure calculations give useful insight into trends between different materials. For the combination with experiments they serve as a road map and guide to identify the character and location of bands.

Acknowledgements

We benefited from fruitful discussions with M. Grioni, R. Claessen, Th. Straub, L. Degiorgi, R. Noack, D. Baeriswyl, and K. Maki. J. Hayoz, M. Bovet, D. Naumović, R. Fasel and L. Schlapbach are gratefully acknowledged for assistance with experiments and calculations and for continuous support. Skillful technical assistance was provided by O. Raetzo, E. Mooser, R. Schmid, O. Zosso, Ch. Neururer, and F. Bourqui. This project has been funded by the Fonds National Suisse pour la Recherche Scientifique.

References

[1] M.R. Halse, Phil. Trans. R. Soc. A265 (1969) 507.
[2] A. Santoni, L.J. Terminello, F.J. Himpsel, T. Takahashi, Appl. Phys. A 52 (1991) 229.
[3] J. Osterwalder, T. Greber, A. Stuck, L. Schlapbach, Phys. Rev. B 44 (1991) 13764.
[4] D. Naumović, A. Stuck, T. Greber, J. Osterwalder, L. Schlapbach, Phys. Rev. B 47 (1993) 7462.
[5] J. Osterwalder, A. Stuck, T. Greber, P. Aebi, L. Schlapbach, S. Hüfner, Vacuum ultraviolet radiation physics, in: F.J. Wuilleumier, Y. Petroff, I. Nenner (Eds.), Proceedings 10th VUV Conference, World Scientific, 1993, p. 475.
[6] P. Aebi, J. Osterwalder, R. Fasel, D. Naumović, L. Schlapbach, Surf. Sci. 307–309 (1994) 917.
[7] P. Aebi, J. Osterwalder, P. Schwaller, L. Schlapbach, M. Shimoda, T. Mochiku, K. Kadowaki, Phys. Rev. Lett. 72 (1994) 2757.
[8] Th. Straub, R. Claessen, P. Steiner, S. Hüfner, V. Eyert, K. Friemelt, E. Bucher, Phys. Rev. B 55 (1997) 13473.
[9] T.J. Kreutz, P. Aebi, J. Osterwalder, Solid State Commun. 96 (1995) 339.
[10] T.J. Kreutz, P. Aebi, J. Osterwalder, L. Schlapbach, J. Electron Spectrosc. Relat. Phenom. 76 (1995) 601.
[11] P. Schwaller, P. Aebi, H. Berger, C. Beeli, J. Osterwalder, L. Schlapbach, J. Electron Spectrosc. Relat. Phenom. 76 (1995) 127.
[12] T.J. Kreutz, T. Greber, P. Aebi, J. Osterwalder, Phys. Rev. B 58 (1998) 1300.
[13] T. Valla, A.V. Fedorov, P.D. Johnson, B.O. Wells, S.L. Hulbert, Q. Li, G.D. Gu, N. Koshizuka, Science 285 (1999) 2110.
[14] Th. Pillo, Ph.D. Thesis, University of Fribourg, Switzerland, 1999.
[15] Th. Pillo, J. Hayoz, H. Berger, M. Grioni, L. Schlapbach, P. Aebi, Phys. Rev. Lett. 83 (1999) 3494.
[16] Th. Pillo, J. Hayoz, H. Berger, F. Lévy, L. Schlapbach, P. Aebi, Phys. Rev. B 61 (2000) 16213.
[17] Th. Pillo, J. Hayoz, H. Berger, R. Fasel, L. Schlapbach, P. Aebi, Phys. Rev. B 62 (2000) 4277.
[18] Th. Pillo, L. Patthey, E. Boschung, J. Hayoz, P. Aebi, L. Schlapbach, J. Electron Spectrosc. Relat. Phenom. 57 (1998) 243.
[19] B. Dardel, M. Grioni, D. Malterre, P. Weibel, Y. Baer, F. Lévy, Phys. Rev. B 45 (1992) 1462.
[20] B. Dardel, M. Grioni, D. Malterre, P. Weibel, Y. Baer, F. Lévy, Phys. Rev. B 46 (1992) 7407.
[21] H. Berger, unpublished.
[22] F. Lévy, Y. Froidevaux, J. Phys. C 12 (1979) 473.
[23] F. Lévy, J. Phys. C 12 (1979) 3725.
[24] F.J. DiSalvo, D.E. Moncton, J.V. Waszczak, Phys. Rev. B 14 (1976) 4321.
[25] P. Aebi, T.J. Kreutz, J. Osterwalder, R. Fasel, P. Schwaller, L. Schlapbach, Phys. Rev. Lett. 76 (1996) 1150.
[26] J. Osterwalder, Surf. Rev. Lett. 4 (1997) 391.
[27] P. Blaha, K. Schwarz, J. Juitz, WIEN97, Vienna University of Technology, 1997, Improved and updated UNIX version of the original copyrighted WIEN code, published by P. Blaha, K. Schwarz, P. Sorantin, S.B. Trickey, in Comput. Phys. Commun., 59 (1990) 399.

[28] J.P. Perdew, S. Burke, M. Ernznerhof, Phys. Rev. Lett. 77 (1996) 3865.
[29] P. Villars, L.D. Calvert, Pearson's Handbook of Crystallographic Data for Intermetallic Phases, American Society for Metals, Metals Park, OH 44073, 1985.
[30] J.A. Wilson, A.D. Yoffe, Adv. Phys. 18 (1969) 193.
[31] R. Claessen, Habilitation, University of Saarbrücken, 1997.
[32] F.J. DiSalvo et al., Solid State Commun. 23 (1977) 825.
[33] R. Claessen, R.O. Anderson, J.W. Allen, C.G. Olson, C. Janowitz, W.P. Ellis, S. Harm, M. Kalnig, R. Manzke, M. Skibowski, Phys. Rev. Lett. 69 (1992) 808.
[34] X. Wu, C. Lieber, Science 243 (1989) 1703.
[35] X. Wu, C. Lieber, Phys. Rev. Lett. 64 (1990) 1150.
[36] P. Fazekas, E. Tosatti, Phil. Mag. B 39 (1979) 229.
[37] P. Fazekas, E. Tosatti, Physica B 99 (1980) 183.
[38] J.W. Gadzuk, Solid State Commun. 15 (1974) 1011.
[39] M.R. Norman, H. Ding, M. Randeria, J.C. Campuzano, T. Yokoya, T. Takeuchi, T. Takahashi, T. Mochiku, K. Kadowaki, P. Guptasarma, D.G. Hinks, Nature 392 (1998) 157.
[40] O. Anderson, R. Manzke, M. Skibowski, Phys. Rev. Lett. 55 (1985) 2188.
[41] A. Zunger, A.J. Freeman, Phys. Rev. B 17 (1978) 1839.
[42] W. Kohn, Phys. Rev. Lett. 19 (1967) 439.